Pure-Supramolecular-Linker Approach to Highly Connected Metal-Organic Frameworks for CO_2 Capture

Xiaohui Song[a‡], Mingxing Zhang[c‡], Cong Chen[a], Jingui Duan[d], Wenwei Zhang[a], Yi Pan[a], and Junfeng Bai*[a,b]

[a] State Key Laboratory of Coordination Chemistry, School of Chemistry and Chemical Engineering, Nanjing University, Nanjing 210023, China

[b] School of Chemistry and Chemical Engineering, Shaanxi Normal University, Xi'an 710119, China

[c] Department of Chemistry, Chongqing Normal University, Chongqing 401331, China

[d] State Key Laboratory of Materials-Oriented Chemical Engineering, College of Chemical Engineering, Nanjing Tech University, Nanjing 210009, China

*Email: bjunfeng@nju.edu.cn; bjunfeng@snnu.edu.cn.

Table of contents

S1. Materials and general methods

General procedures. All chemical reagents were obtained from commercial sources and, unless otherwise noted, were used as received without further purification. Elemental analyses (C, H, N) were carried out on a Perkin-Elmer 240 analyzer. *In situ* FTIR (Fourier Transform Infrared Spectroscopy) spectra were collected in the 4000~600 cm^{-1} on a Bruker Tensor 27 spectrometer using KBr pellets with heating rate 20 °C/min. DRIFTS (Diffuse Reflectance Infrared Fourier Transform Spectroscopy) spectra were collected in the 4000~600 cm^{-1} on a Nicolet 5700 FTIR spectrometer with a liquid N_2 cooled detector. ^1H NMR spectra were recorded on a Bruker DRX-300 spectrometer with tetramethylsilane as an internal reference. Thermal gravimetric analyses (TGA) were performed under N_2 atmosphere (100 mL min^{-1}) with a heating rate of 20 °C min^{-1} using a 2960 SDT thermogravimetric analyzer. Powder X-ray diffraction (PXRD) data were collected on a Bruker D8 ADVANCE X-ray diffractometer with Cu/Kα radiation. X-ray photoelectron spectroscopy (XPS) spectra were recorded using a PHI 5000 VersaProbe instrument. Gas sorption measurements were conducted using a Micrometritics ASAP 2020 surface area and pore size analyzer up to saturated pressure at different temperatures. Water stability measurements were carried out by directly immersing the as-synthesized samples into pure water or aqueous solutions with various pH values, and then samples were obtained for PXRD and N_2 adsorption measurements after a period of time.

1.1 Ligand synthesis

The organic linker N, N', N''-Tris(isophthalyl)-1,3,5-benzenetricarboxamide (TPBTM) was prepared according to literatures[1] and characterized by IR and ^1H NMR. Selected IR (KBr, cm^{-1}): 3078, 2662, 2570, 1835, 1711, 1652, 1608, 1556, 1451, 1430, 1407, 1336, 1270, 1245, 1229, 1107, 1059, 1018, 1002, 977, 909, 757, 727, 688, 664. ^1H NMR (DMSO-d_6, δ ppm): 13.36 (broad peak, COOH), 10.97 (s, 3H,

CONH), 8.85 (s, 3H, ArH), 8.74 (s, 6H, ArH), 8.26 (s, 3H, ArH).

1.2 Synthesis of $\{Fe_3O(TPBTM^{6-})(Cl^-)(H_2O)_2\}_\infty$ (NJU-Bai52)

A mixture of $FeCl_3 \cdot 6H_2O$ (5.8 mg, 0.021 mmol), TPBTM (10 mg, 0.014 mmol), CH_3COOH (0.8 mL) and 2 mL DMF was sealed in a 20 mL Pyrex tube, which was heated to 130 °C for 5 days. After cooling to the room temperature, the brown block crystals were obtained. The crystals of NJU-Bai52 were filtered and washed with DMF. Yield 10.0 mg. Selected IR (cm^{-1}): 3417, 3258, 3072, 2929, 2874, 2355, 1662, 1622, 1578, 1549, 1423, 1374, 1359, 1282, 1240, 1167, 1098, 1060, 1003, 964, 908, 867, 802, 777, 713, 663, 633. Anal. Calcd (Found), $C_{51}H_{66}O_{26.5}N_9Cl_1Fe_3$: C, 42.73 (42.77); H, 4.74 (4.64); N, 9.00 (8.80)%.

1.3 Synthesis of $\{Sc_3O(TPBTM^{6-})(OH^-)(H_2O)_2\}_\infty$ (NJU-Bai53)

A mixture of $ScCl_3 \cdot 6H_2O$ (10 mg, 0.043 mmol), TPBTM (20 mg, 0.029 mmol), HNO_3 (3.5 mol/L, 1.6 mL) and 5 mL DMF was sealed in a 20 mL Pyrex tube, which was heated to 130 °C for 2 days. After cooling to the room temperature, the colorless block crystals were obtained. The crystals of NJU-Bai53 were filtered and washed with DMF. Yield 9.2 mg. Selected IR (cm^{-1}): 3266, 3078, 2939, 2878, 1667, 1627, 1583, 1553, 1431, 1384, 1281, 1238, 1098, 1061, 1004, 988, 963, 909, 869, 780, 711, 691, 663, 627. Anal. Calcd (Found), $C_{45}H_{52}O_{25}N_7Sc_3$: C, 44.23 (44.09); H, 4.46 (4.28); N, 7.77 (7.99)%.

S2. Single-crystal X-ray structure determination

Single-crystal X-ray diffraction data were measured on a Bruker D8 Venture diffractometer using graphite monochromated Mo/Kα radiation (λ = 0.71073 Å). Data reduction was made with the Bruker SAINT program. The structures were solved by direct methods and refined with full-matrix least squares technique using the

SHELXTL package[2]. Non-hydrogen atoms were refined with anisotropic displacement parameters during the final cycles. Organic hydrogen atoms were placed in calculated positions with isotropic displacement parameters set to 1.2 × U_{eq} of the attached atom. The hydrogen atoms of the ligated water molecules could not be located. The unit cell includes a large region of disordered solvent molecules, which could not be modelled as discrete atomic sites. We employed PLATON/SQUEEZE[3] to calculate the diffraction contribution of the solvent molecules and, thereby, to produce a set of solvent-free diffraction intensities; structures were then refined again using the data generated.

A summary of the crystallographic data are given in Table S1. CCDC 1936061 and 1936060 contain the supplementary crystallographic data for **NJU-Bai52** and **NJU-Bai53**. The data can be obtained free of charge at www.ccdc.cam.ac.uk/conts/retrieving.html or from the Cambridge Crystallographic Data Centre, 12, Union Road, Cambridge CB2 1EZ, UK.

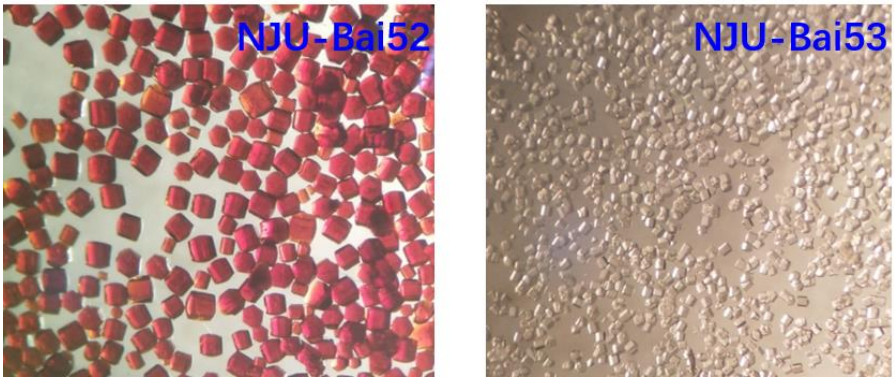

Figure S1. Optical microscope images of crystals of **NJU-Bai52** and **NJU-Bai53**.

Table S1. Crystallographic data and structure refinement results for **NJU-Bai52** and **NJU-Bai53**.

MOFs	**NJU-Bai52**	**NJU-Bai53**
CCDC number	1936061	1936060
Empirical formula	$C_{33}H_{15}Fe_3N_3O_{19}Cl$	$C_{35}H_{15}Sc_3N_3O_{20}$
Formula weight	960.48	932.38
Temperature/K	153	153
Crystal system	Trigonal	Trigonal
Space group	*P*$\bar{3}$*m1*	*P*$\bar{3}$*m1*
***a* (Å)**	26.742(3)	27.121(8)
***b* (Å)**	26.742(3)	27.121(8)
***c* (Å)**	16.8667(19)	17.508(6)
***α* (°)**	90	90
***β* (°)**	90	90
***γ* (°)**	120	120
***V* (Å^3)**	10446(3)	11153(8)
Z	6	6
D_{calcd} **(g cm^{-3})**	0.916	0.833
***μ*/mm^{-1}**	0.702	0.312
F(000)	2886.0	2814.0
Crystal size [mm^3]	0.3 x 0.2 x 0.1	0.12 x 0.12 x 0.02
Theta range [deg]	2.327 – 26.365	2.088 – 25.013
Limiting indices	-33 < = h < = 33	-24 < = h < = 32
	-31 < = k < = 33	-32 < = k < = 31
	-21 < = l < = 18	-20< = l < = 20
Reflns collected	7485	7025
Reflns unique	2732	4676
Completeness	98.3%	99.9%
Data/restraints/parameters	7485 / 46 / 261	7025 / 227 / 265
Goodness-of-fit on F^2	1.101	1.373
R1, wR2[a] [I > 2σ(I)]	0.1340, 0.3683	0.1623, 0.4097
R1, wR2 [all data]	0.2076, 0.4112	0.1909, 0.4305
$\Delta\rho_{max}$ / $\Delta\rho_{min}$[e. Å^{-3}]	1.789, -0.914	1.695 / -0.781

[a] $R1 = \Sigma||F_o| - |F_c||/|F_o|$; $wR2 = [\Sigma w(\Sigma F_o^2 - F_c^2)^2/\Sigma w(F_o^2)^2]^{1/2}$.

S3. The structures of NJU-Bai52 and NJU-Bai53

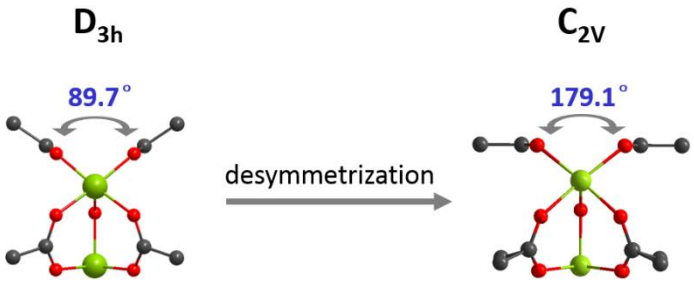

Figure S2. The dihedral angle between the two carboxylate moieties bridging Fe2 and Fe3 extends from usual 90° to 180°, which degrades the symmetry of Fe_3O cluster from familiar D_{3d} to C_{2v} without the variation of the connectivity.

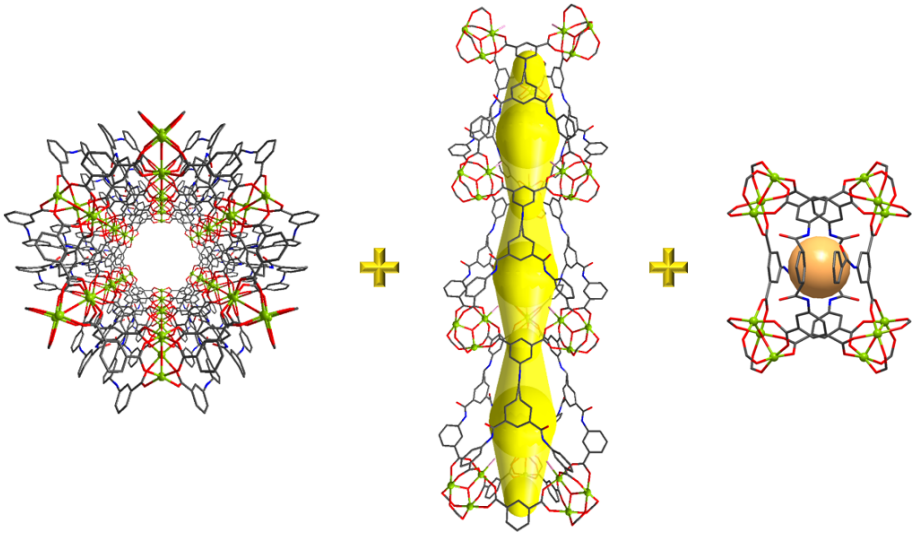

Figure S3. NJU-Bai52 consists of three different types of pores: the 1D hexagonal nanotube size is 10.4 Å (NJU-Bai53, 9.7 Å) around the metallamacrocycle and 14.6 Å (NJU-Bai53, 14.6 Å) for maximum diameter, the hourglass-shaped nanotube has a window size of diameter 3.7 Å (NJU-Bai53, 3.4 Å), and the octahedron cage with an accessible diameter of about 6.5 Å (NJU-Bai53, 6.7 Å).

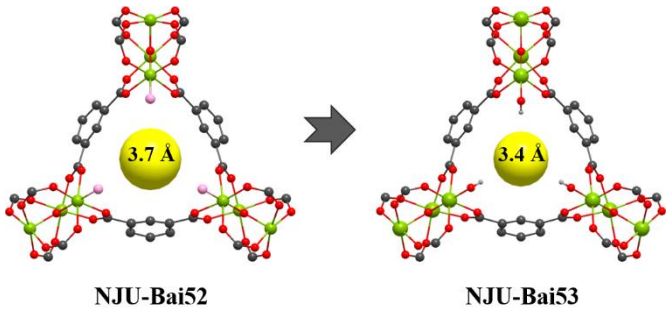

Figure S4. The triangular window of the 1D hourglass-shaped nanotube. Compared with 3.7 Å for NJU-Bai52, the window size of NJU-Bai53 decreases to 3.4 Å, which is quite close to the kinetic diameter of carbon dioxide (3.3 Å), enhancing the interaction between the framework and CO_2 molecule.

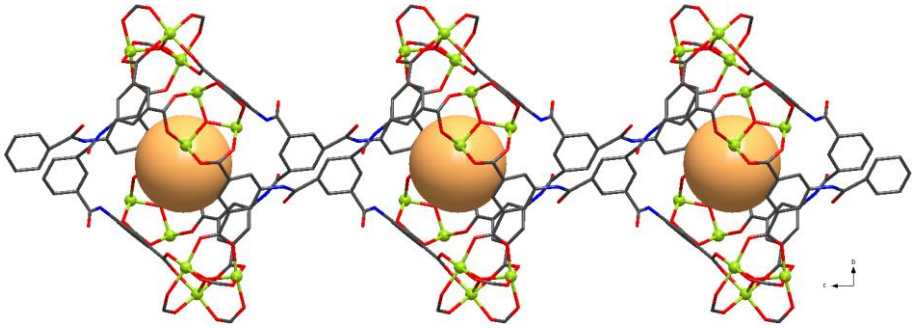

Figure S5. The stacking pattern between octahedral cages.

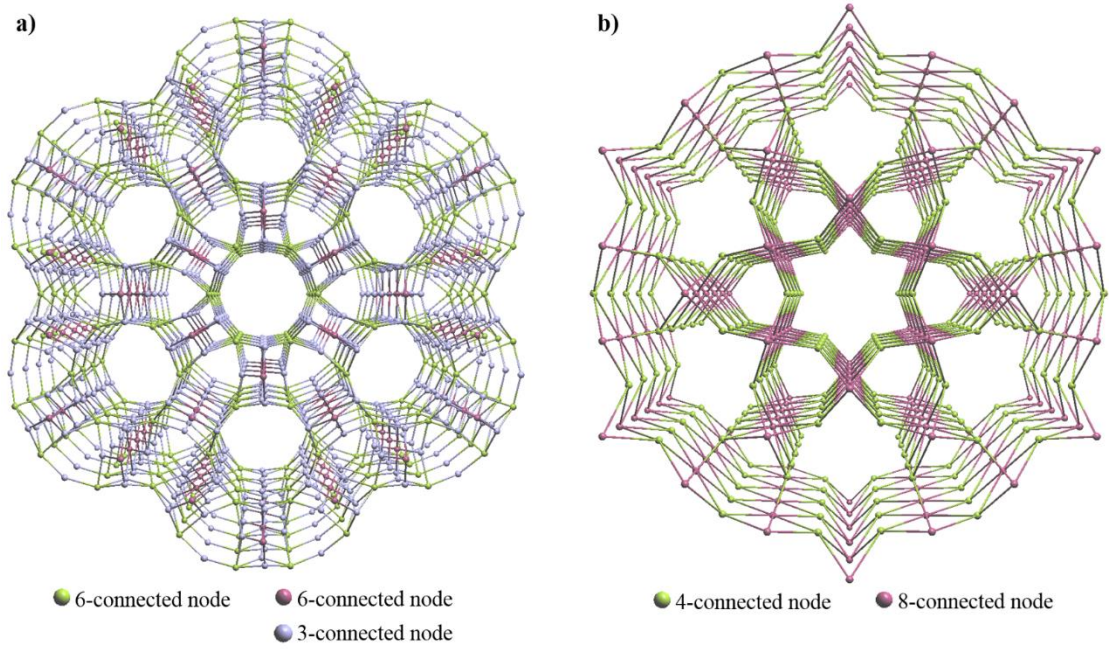

Figure S6. a) The topological network of NJU-Bai52 with the Schläfli symbol of $(4^2•6)_6(4^4•6^2•8^6•10^3)(4^4•6^3•8^6•10^2)_2$, in which the Fe_3O cluster is simplified as a

6-connected node, and the PSL is reduced to 6-connected node and the peripheral isophthalate is considered as 3-connected node. b) Alternatively, each Fe_3O cluster connects four PSLs being regarded as a 4-connected node, and each PSL bridges eight Fe_3O clusters through its 12 carboxylate groups being actually regarded as an 8-connected node. As a result, The framework could be simplified as a (4,8)-c network with a **csq** topology.

S4. Powder X-ray diffraction patterns

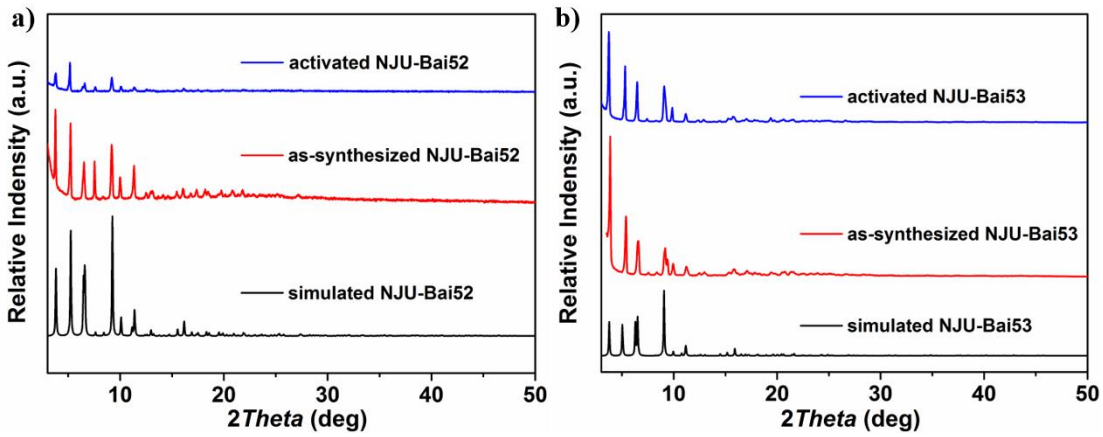

Figure S7. The PXRD patterns of **NJU-Bai52** (a) and **NJU-Bai53** (b).

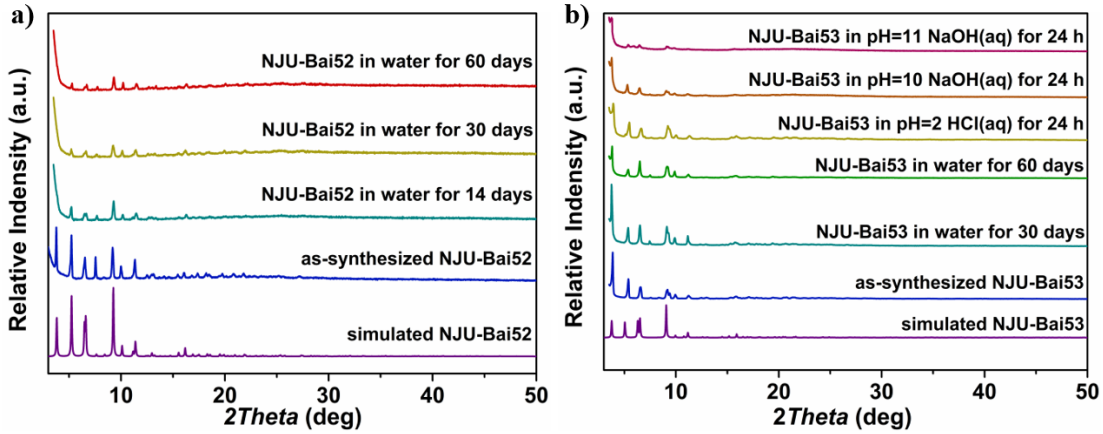

Figure S8. The PXRD patterns of **NJU-Bai52** (a) and **NJU-Bai53** (b) after different treatments, respectively.

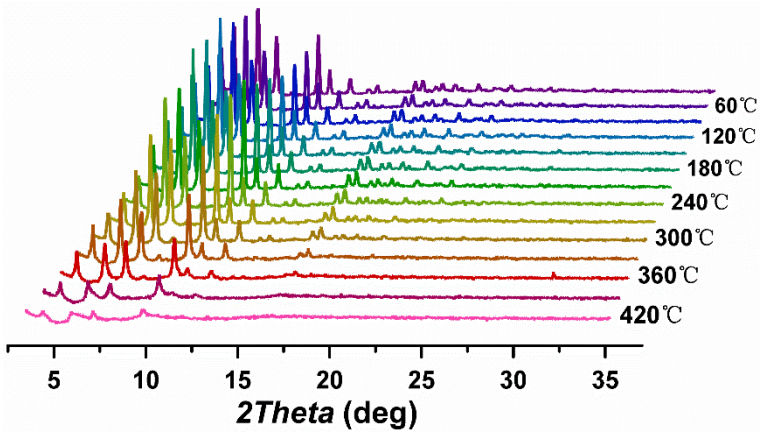

Figure S9. VT-PXRD patterns of as-synthesized sample of **NJU-Bai52** under vacuum.

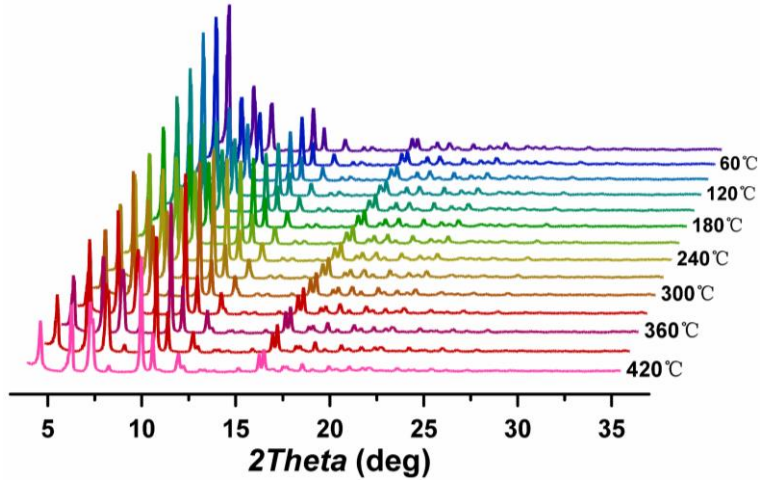

Figure S10. VT-PXRD patterns of as-synthesized sample of **NJU-Bai53** under vacuum.

S5. Thermogravimetric analysis curves

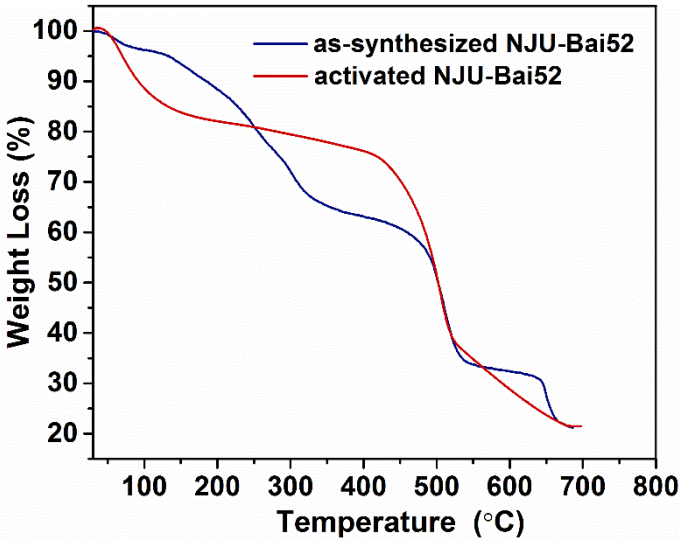

Figure S11. TGA curves of as-synthesized (dark blue) and activated (red) **NJU-Bai52**.

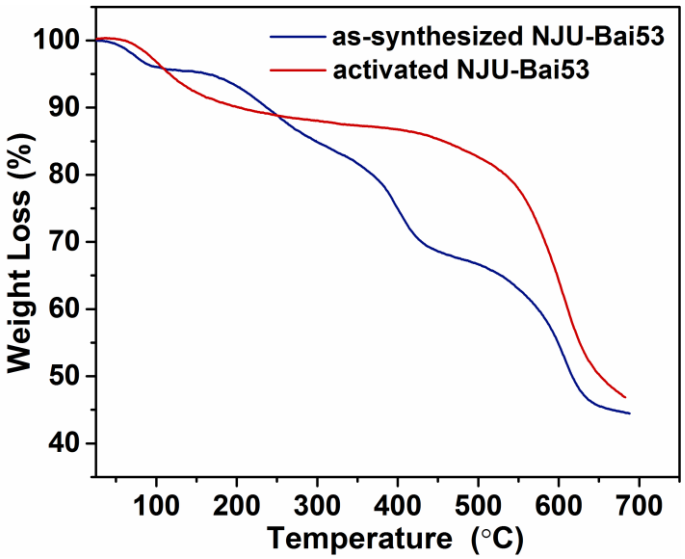

Figure S12. TGA curves of as-synthesized (dark blue) and activated (red) **NJU-Bai53**.

S6. *In situ* FTIR spectra

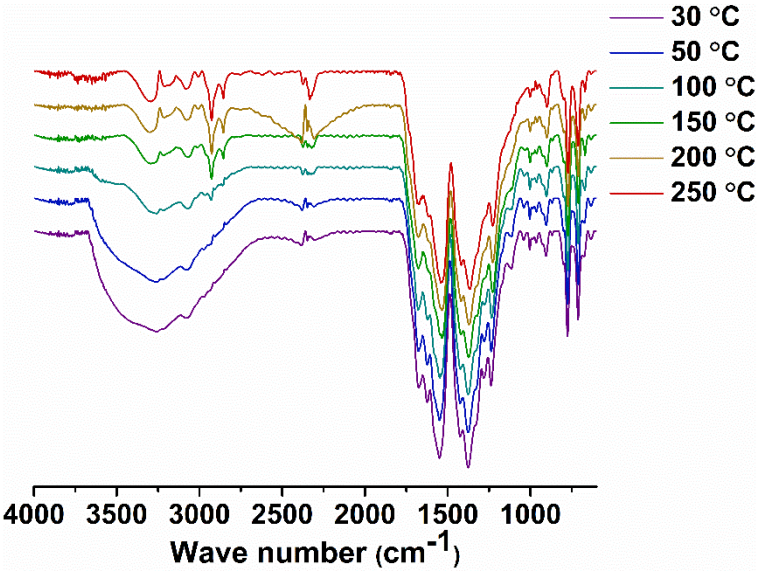

Figure S13. *In situ* FTIR spectra of the CH_3OH-exchanged sample **NJU-Bai52** at various temperatures under vacuum.

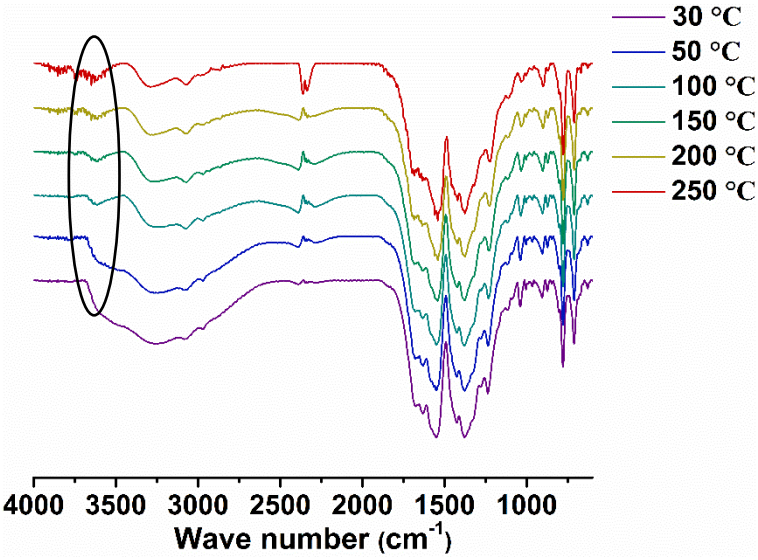

Figure S14. *In situ* FTIR spectra of the CH_3OH-exchanged sample **NJU-Bai53** at various temperatures under vacuum, which shows the peaks attributed to coordinated hydroxide.[4]

S7. DRIFTS spectra

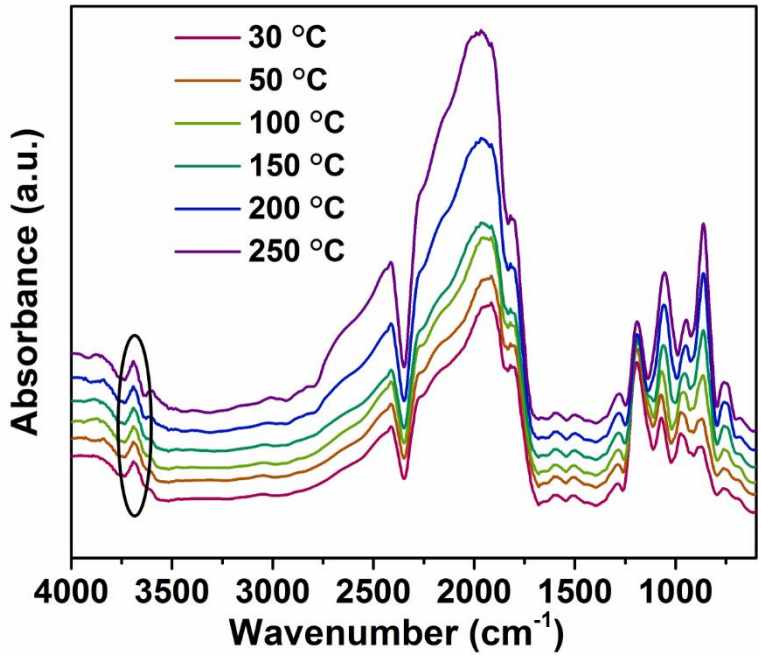

Figure S15. The DRIFTS spectra of the CH_3OH-exchanged sample **NJU-Bai53** at various temperatures under flowing argon, in which the peaks appear at around 3670 cm^{-1} attributed to coordinated hydroxide.

S8. XPS spectra

The solvent-exchanged samples (**NJUBai52** and **NJU-Bai53**) were activated at 170 ˚C under vacuum for 12 hours. Then, the activated samples are transferred to a PHI 5000 VersaProbe instrument for XPS analyses. As shown in Figure S14, XPS analyses confirm the presence of chloride in the activated sample **NJUBai52** and the absence of chloride in the activated sample **NJUBai53**. The relative atomic percentages measured are shown in Tables S2. The ratio of Fe/Cl according to their relative atomic percentages is calculated to be 3.3, which is almost consistent with one Cl^- anion per cluster.

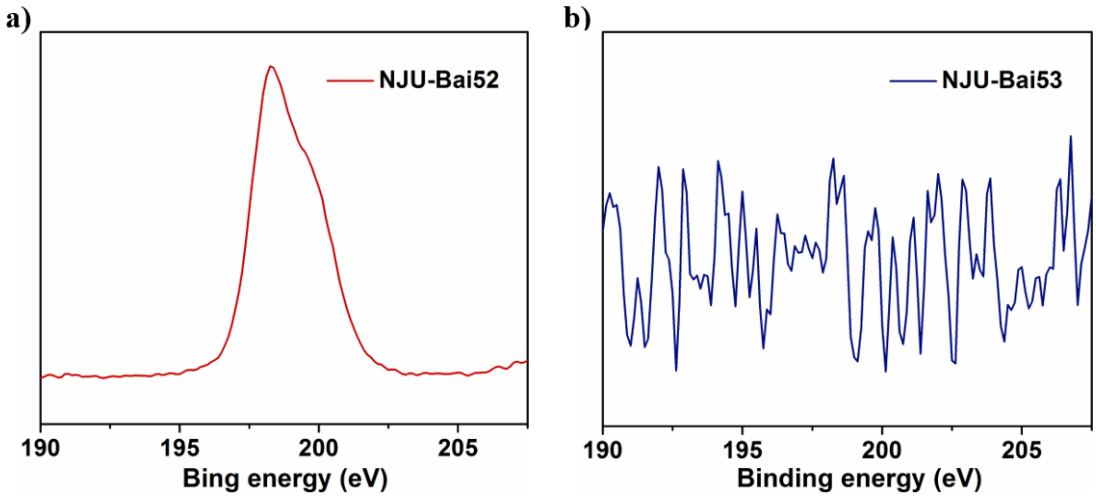

Figure S16. Cl 2p XPS spectra of **NJU-Bai52** (a) and **NJU-Bai53** (b).

Table S2. Atomic percentage of Cl in the activated sample **NJUBai52**.

	Atomic %
C 1s	62.96
N 1s	6.83
Cl 2p	4.75
Fe 2p	25.46

Table S3. Atomic percentage of Cl in the activated sample **NJUBai53**.

	Atomic %
C 1s	69.81
N 1s	7.04
Cl 2p	0.00
Sc 2p	23.15

S9. Low-pressure gas sorption measurements

Sample activation. Before sorption experiment, as-synthesized **NJU-Bai52** samples were soaked in dry methanol for 3 days with methanol refreshing every 8 hours. The as-synthesized samples of **NJU-Bai53** were soaked in dry CH_2Cl_2 for 3 days with CH_2Cl_2 refreshing every 8 hours. After that, CH_2Cl_2 is decanted and sample is soaked in dry methanol for 3 days with methanol refreshing every 8 hours. Then, the solvent-exchanged samples (**NJUBai52** and **NJU-Bai53**) were activated at 170 ℃ under vacuum for 12 hours.

Low-pressure gas (N_2, CO_2, CH_4) sorption isotherms (up to 1 bar) were performed on Micromeritics ASAP 2020 M+C surface area and pore size analyzer. Before gas sorption measurements, about 400 mg samples were activated by using the "outgas" function of the surface area analyzer. For all isotherms, warm and cold free space correction measurements were performed using ultra-high purity He gas (UHP grade 5.0, 99.999% purity). The specific surface areas were determined using the Brunauer-Emmett-Teller (BET) and the Langmuir equation from the N_2 sorption data at 77 K. When applying the BET theory, we made sure that our analysis satisfied the two consistency criteria as detailed by Walton and co-workers[5]. For the Langmuir surface area, data from the whole adsorption data were used. The pore size distribution (PSD) was obtained from the DFT model in the Micromeritics ASAP2020 software package based on the N_2 sorption isotherm.

The wt% gas uptake is defined by equation (1):

$$wt\% = (100 \times N) / (1000 + N) \qquad (1)$$

in which N is excess (or total) adsorption (N_{exc} or N_{tot}, mg g^{-1}).

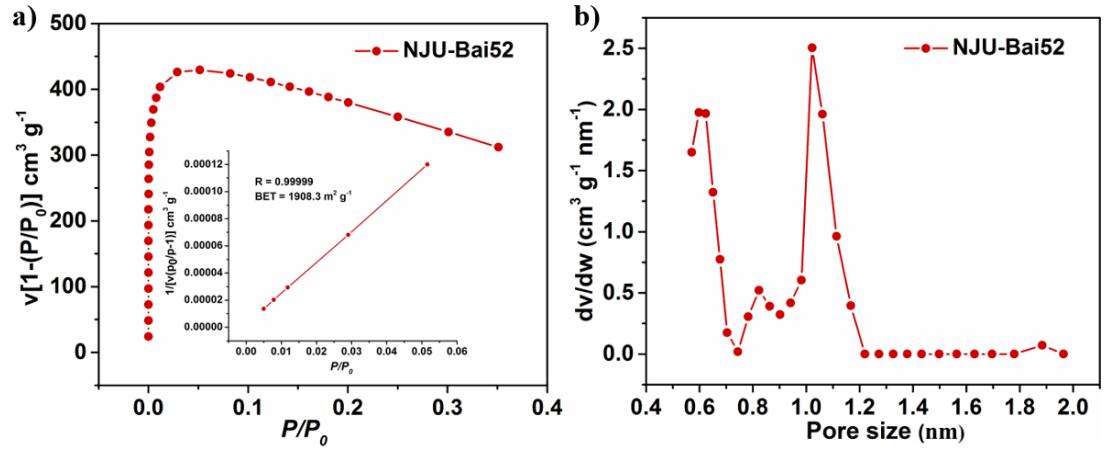

Figure S17. a) V[1-(P/P$_0$)] vs P/P$_0$ for **NJU-Bai52**, only the range below P/P$_0$ = 0.03 satisfies the first consistency criterion for applying the BET theory. Inset: Plot of the linear region for the BET equation. b) The pore size distribution curve of **NJU-Bai52**.

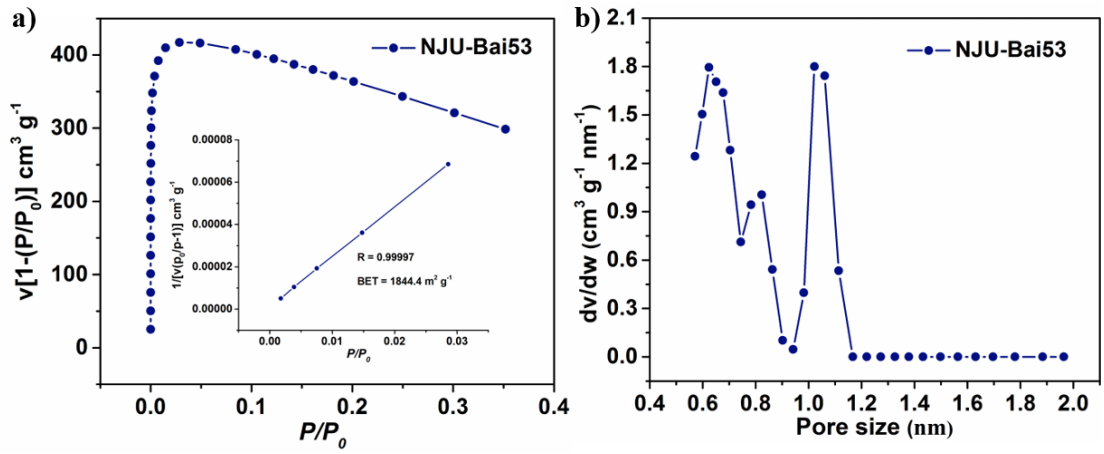

Figure S18. a) V[1-(P/P$_0$)] vs P/P$_0$ for **NJU-Bai53**, only the range below P/P$_0$ = 0.03 satisfies the first consistency criterion for applying the BET theory. Inset: Plot of the linear region for the BET equation. b) The pore size distribution curve of **NJU-Bai53**.

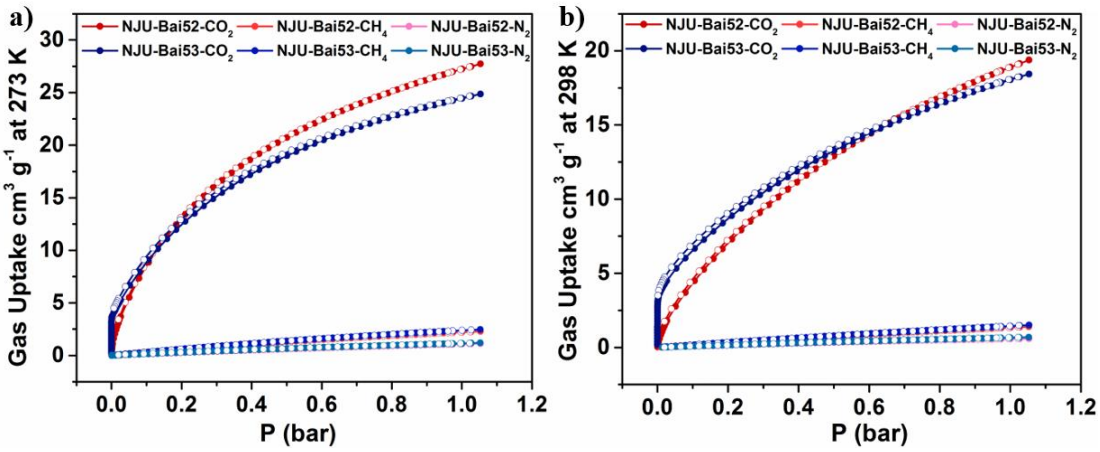

Figure S19. CO_2, CH_4, and N_2 adsorption (closed) /desorption (open) isotherms for **NJU-Bai52** and **NJU-Bai53** at 273 K (a) and 298 K (b), respectively.

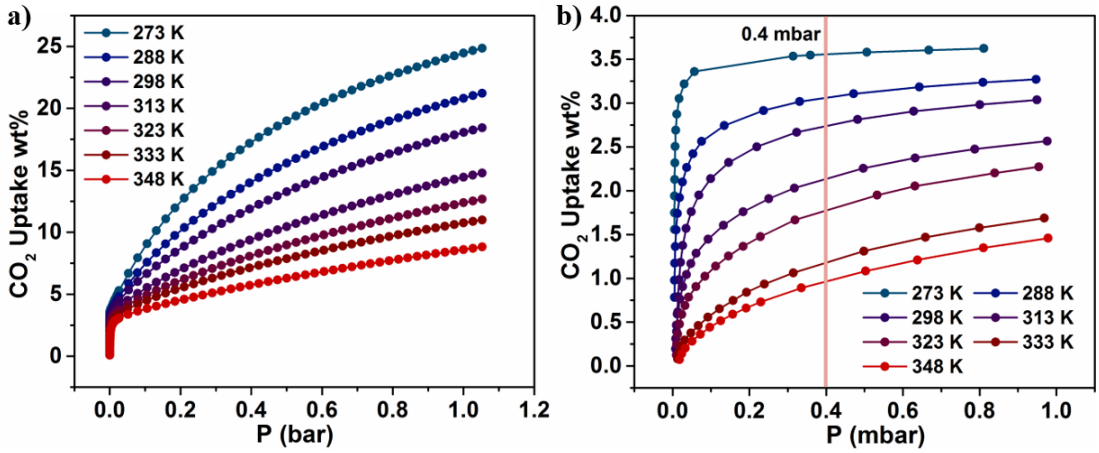

Figure S20. a) CO_2 adsorption isotherms for **NJU-Bai53** at different temperatures. b) The isotherms at very low pressures.

S10. Calculations of isosteric heat of adsorption (Q_{st})

A virial-type[6] expression comprising the temperature-independent parameters a_i and b_j was employed to calculate the enthalpies of adsorption for CO_2 and CH_4 (at 273, 298 and 313 K) on **NJU-Bai52** and **NJU-Bai53**. In each case, the data were fitted using the equation (2):

$$\ln P = \ln N + 1/T \sum_{i=o}^{m} a_i N^i + \sum_{j=0}^{n} b_j N^j \quad (2)$$

Here, P is the pressure expressed in Torr, N is the amount adsorbed in mmol g^{-1}, T is the temperature in K, a_i and b_j are virial coefficients, and m, n represent the number of coefficients required to adequately describe the isotherms (m and n were gradually increased until the contribution of extra added a and b coefficients was deemed to be statistically insignificant towards the overall fit, and the average value of the squared deviations from the experimental values was minimized). The values of the virial coefficients a_0 through a_m were then used to calculate the isosteric heat of adsorption using the following expression (3).

$$Q_{st} = -R \sum_{i=0}^{m} a_i N^i \quad (3)$$

Q_{st} is the coverage-dependent isosteric heat of adsorption and R is the universal gas constant. The heats of CO_2 and CH_4 sorption for **NJU-Bai52** and **NJU-Bai53** in the manuscript are determined by using the low pressure gas sorption data measured in the pressure range from 0-1 bar (273, 298 and 313 K), which is fitted by the virial-equation very well.

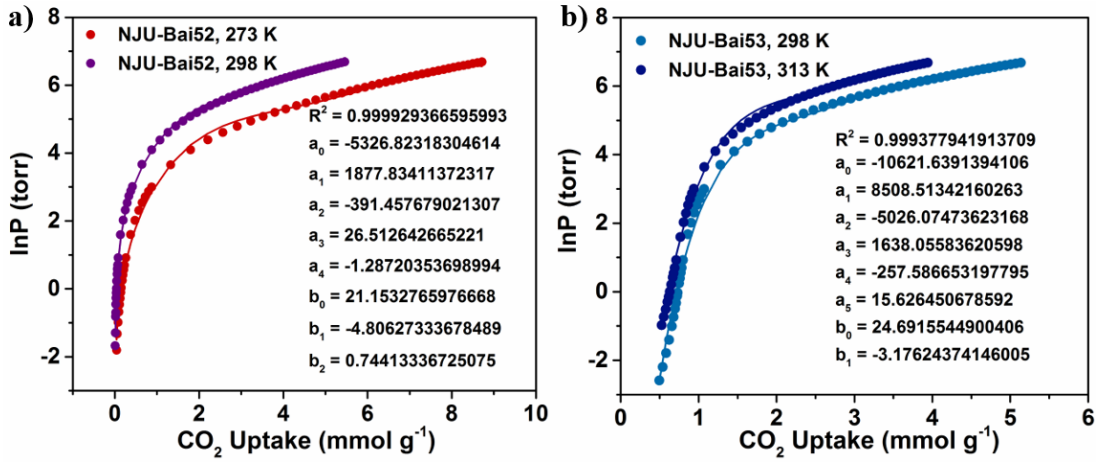

Figure S21. a, b) The details of virial equation (solid lines) fitting to the experimental CO_2 adsorption data (symbols) for **NJU-Bai52** and **NJU-Bai53**, respectively.

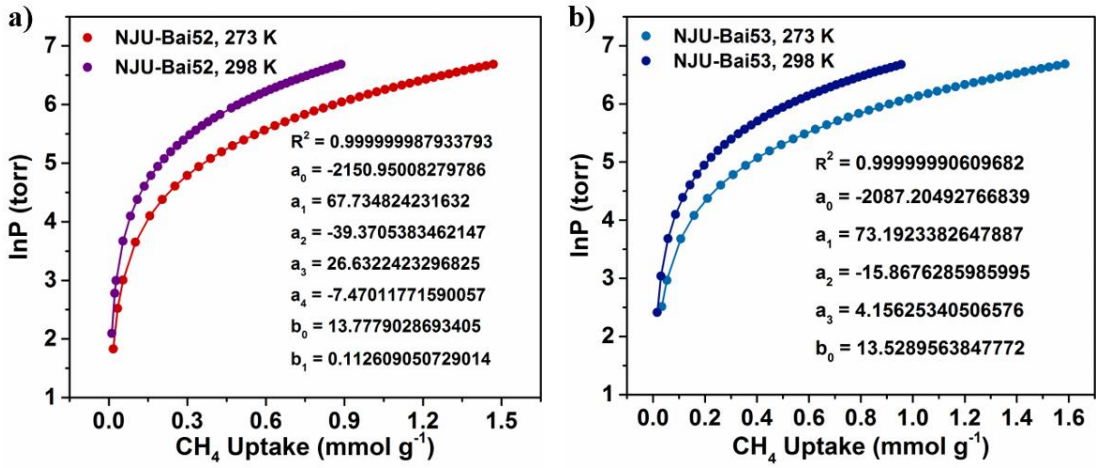

Figure S22. a, b) The details of virial equation (solid lines) fitting to the experimental CH_4 adsorption data (symbols) for **NJU-Bai52** and **NJU-Bai53**, respectively.

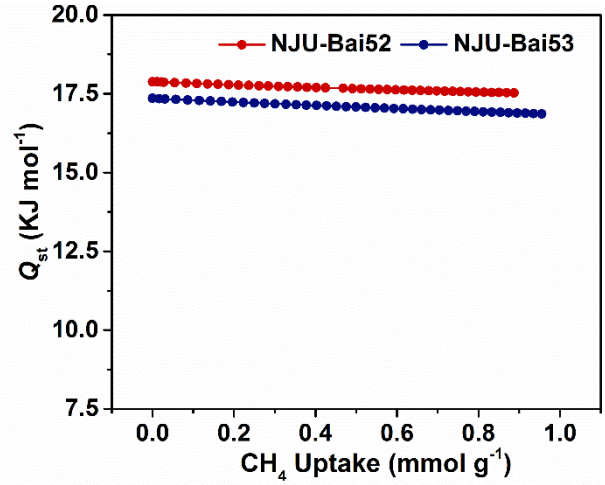

Figure S23. The isosteric CH_4 adsorption enthalpies of **NJU-Bai52** and **NJU-Bai53**.

S11. IAST calculations

IAST (ideal adsorption solution theory)[7] was used to predict binary mixture adsorption from the experimental pure-gas isotherms. In order to perform the integrations required by IAST, the singlecomponent isotherms should be fitted by a proper model. In practice, several methods to do this are available. We found for this set of data that the dual-site Langmuir-Freundlich equation was successful in fitting the data. As can be seen in Figure S21-22 and Table S2-3, the model fits the isotherms very well ($R^2 > 0.9999$).

$$q = \frac{q_{m,1} b_1 p^{1/n_1}}{1 + b_1 p^{1/n_1}} + \frac{q_{m,2} b_2 p^{1/n_2}}{1 + b_2 p^{1/n_2}} \quad (4)$$

Here, P is the pressure of the bulk gas at equilibrium with the adsorbed phase (kPa), q is the adsorbed amount per mass of adsorbent (mmol g^{-1}), $q_{m,1}$ and $q_{m,2}$ are the saturation capacities of sites 1 and 2 (mmol g^{-1}), b_1 and b_2 are the affinity coefficients of sites 1 and 2 (1/kPa), and n_1 and n_2 represent the deviations from an ideal homogeneous surface. The fitted parameters were then used to predict multi-component adsorption with IAST.

The selectivity $S_{A/B}$ in a binary mixture of components A and B is defined as $(x_A/y_A)/(x_B/y_B)$, where x_i and y_i are the mole fractions of component i (i = A , B) in the adsorbed and bulk phases, respectively.

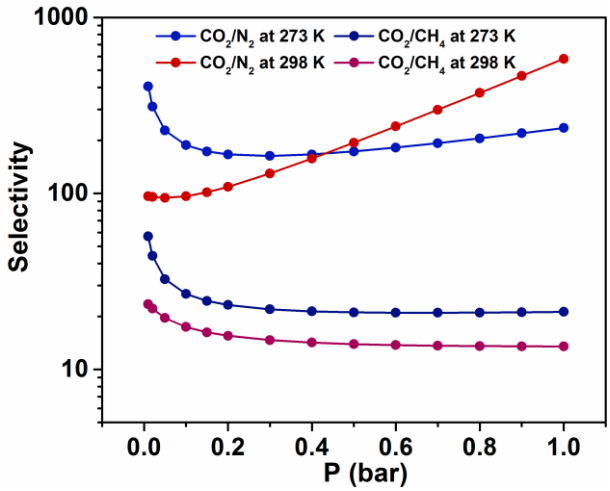

Figure S24. IAST predicted selectivity for CO_2/N_2 (15/85) and CO_2/CH_4 (50/50) mixture of **NJU-Bai52** at 273 K and 298K.

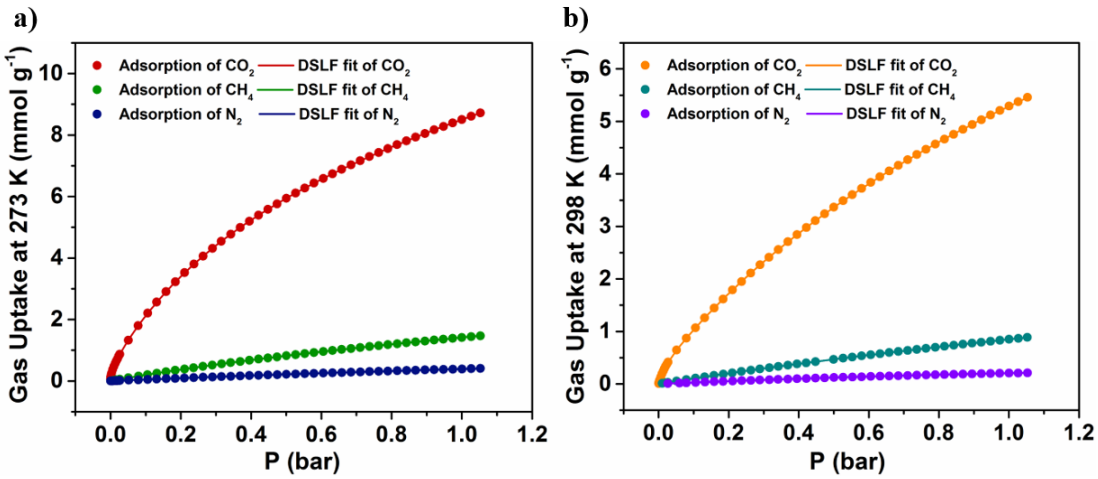

Figure S25. a, b) Low pressure gas adsorption isotherms and the dual-site Langmuir-Freundlich (DSLF) fit lines of CO_2, N_2 and CH_4 in **NJU-Bai53** at 273 K and 298 K, respectively.

Table S4. Dual-site Langmuir-Freundlich parameters for pure CO_2, N_2 and CH_4 isotherms in **NJU-Bai52** at 273 K

	NJU-Bai52		
	CO_2	N_2	CH_4
R^2	0.999997599886581	0.999999823704895	0.999999971665649
$q_{m,1}$	9997.49508421439	0.00186261162301977	8.04530101400979
$q_{m,2}$	2.46730683537989	1.7974482967967	1.10288574912569
b_1	4.58247581374847E-5	0.195123029243127	0.00108855350825509
b_2	0.0073367327009631	0.00236329693083056	0.0107721079722001
n_1	0.572921025849642	1.78182298262981	1.01994785573232
n_2	1.40813904036138	1.03044626134288	0.97650310882619

Table S5. Dual-site Langmuir-Freundlich parameters for pure CO_2, N_2 and CH_4 isotherms in **NJU-Bai52** at 298 K

	NJU-Bai52		
	CO_2	N_2	CH_4
R^2	0.999998051500304	0.999998845936279	0.9999999325815
$q_{m,1}$	14.8371366681511	0.275697273845328	9.49056622311807
$q_{m,2}$	0.269170730053418	0.149327125566197	0.435412599945871
b_1	0.00620983018840104	0.00981161566531046	0.000863872074231023
b_2	0.654344891277494	0.000214449351712522	0.00575417582549132
n_1	0.955381825581378	1.00811841319563	0.964557654288662
n_2	1.02763736346635	1.77164990185463	1.06930462915619

S12. Molar selectivity calculations

Since we were unable to mathematically model the CO_2 isotherms of NJU-Bai53 with a meaningful, single equation over the entire pressure range of interest, IAST selectivities could not be calculated. We applied the simple selectivity equation $S = (q_1/q_2)/(p_1/p_2)$, where the adsorption capacities of component n (q_n) are defined to be molar excess adsorption capacities determined experimentally without correction for absolute adsorption, and p_n is defined to be the pressure of component n as experimentally measured.

Table S6. BET surface areas, CO_2 uptakes, CO_2 enthalpies, and CO_2 selectivities of **NJU-Bai52**, **NJU-Bai53**, and some famous MOFs at 298 K

MOFs	Surface area[a] ($m^2\ g^{-1}$)	CO_2 uptake (wt %)			$Q_{st,\ CO2}$ ($kJ\ mol^{-1}$)	Selectivity[b]		Ref.
		0.4 mbar	0.15 bar	1 bar		CO_2/N_2	CO_2/CH_4	
NJU-Bai52	**1908**	**0.057**	**5.75**	**18.9**	**44.2**	**581/147[c]/41[d]**	**13.5**	
NJU-Bai53	**1844**	**2.74**	**7.67**	**18.1**	**88.3**	**6397[c]/50[d]**		
NJU-Bai7	1155		7.42		40.5	70[d]		8
SIFSIX-2-Cu-i	735	0.30	9.19	19.2	31.9	140	33	9
Mg-MOF-74	1495	0.39	21.16	26.0	47	182.1		10
MAF-X25ox	1286[e]	4.01	15.00	23.9	90	250[d]		11
MAF-X27ox	1167[e]	4.73	15.28	22.7	110	262[d]		11
NJU-Bai35	862.8		7.20	14.6	33.37	275.8	11.6	12
UTSA-16	628		9.44	15.9	34.6	314.7		10c
mmen-CuBTTri	870	0.22	9.48	15.4	96	327		13
NJU-Bai51	1280	0.56	3.81	12.3	33.3	545.7	10.7	14
SIFSIX-3-Zn	250[f]	0.57	9.66	10.1	45	1818	231	9
SIFSIX-3-Cu	300[f]	5.17	9.33		54	>25000		15
mmen-Mg_2(dobpdc)	70	8.09	12.10	14.5	71	49000[c]/200[d]		16
en-Mg_2(dobpdc)	1253	11.07	13.74	16.7	51	70000[c]/230[d]		17

[a] BET surface areas calculated from N_2 isotherms at 77 K unless otherwise stated. [b] Selectivity obtained from IAST calculations unless specially noted. [c] Molar selectivity of CO_2/N_2 (0.4/800) in air. [d] Molar selectivity of CO_2/N_2 (15/75) in flue gas. [e] Langmuir surface area. [f] Calculated from 298 K CO_2 isotherm.

S13. Adsorption stability tests

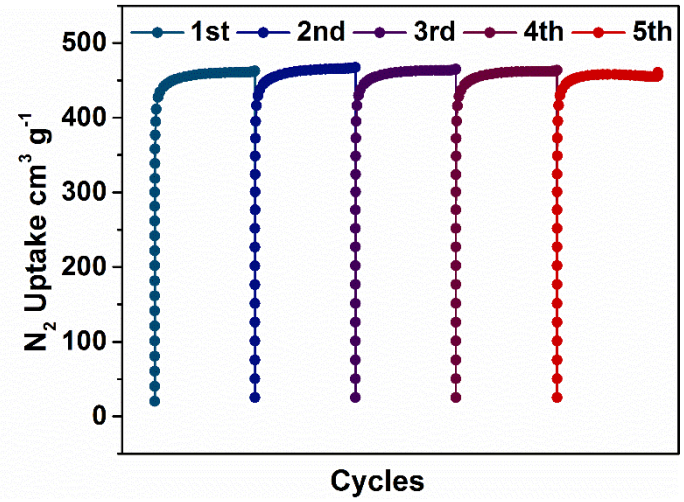

Figure S26. Five cycles of N_2 uptake in **NJU-Bai53** at 77 K. Data was collected with a Micrometritics ASAP 2020 analyzer.

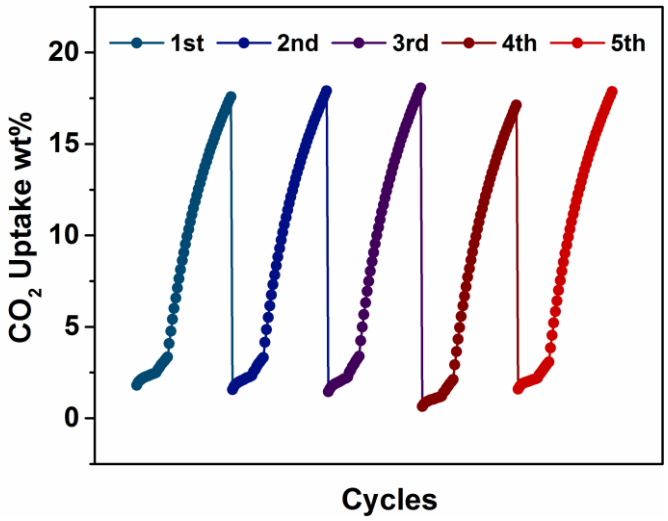

Figure S27. Five cycles of CO_2 uptake in **NJU-Bai53** at 298 K. The sample **NJU-Bai53** was regenerated at 80 °C under dynamic vacuum for 3 h after measurement of each isotherm. The gas uptake decreased very a little in the fourth cycle because the sample was not regenerated before this test. Once regenerated according to the above conditions, such as the fifth cycle, CO_2 uptake fully recovered. Data was collected with a Micrometritics ASAP 2020 analyzer.

S14. N_2 adsorption after water treatments

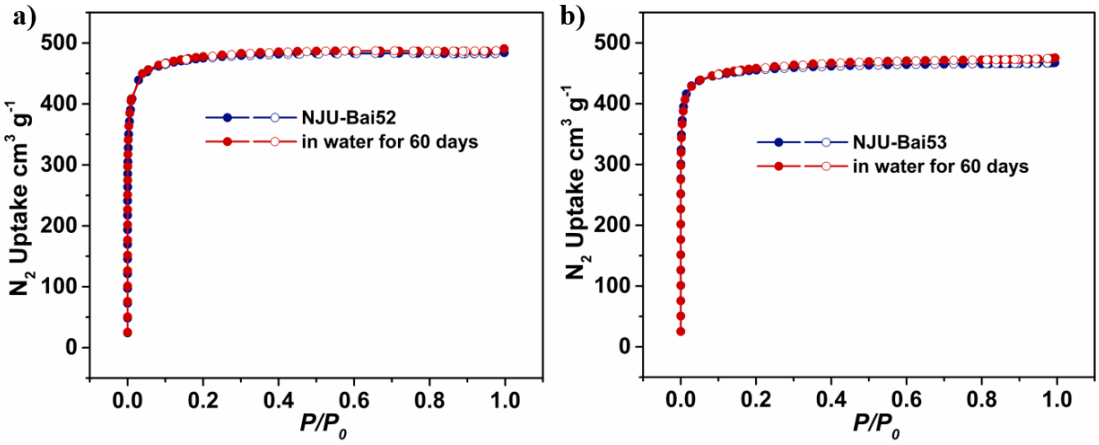

Figure S28. N_2 adsorption (closed) / desorption (open) isotherms of water-treated **NJU-Bai52** (a) and **NJU-Bai53** (b), respectively.

S15. Breakthrough experiments

Breakthrough system used in this study is hand-made according to the literatures[18]. The flow rates of all gases are regulated by mass flow controllers, and the effluent gas stream from the column is monitored by a gas chromatography (GC). All measurements were performed following a protocol established by the literatures[18a-c]. Activated sample **NJU-Bai52** (450 mg) or **NJU-Bai53** (490 mg) was packed into a stainless-steel column (12 cm length × 0.30 cm internal diameter) and the remaining volume in the column was filled by glass wool. The packed column was initially purged with helium gas for 30 mins until no other gases were detected in the effluent. Then, a CO_2 flow and N_2 flow (total is 10 mL min^{-1}: 15/85), a CO_2 flow and CH_4 flow (total is 10 mL min^{-1}: 50/50) were dosed into the column. A breakthrough of CO_2 was determined when the concentration of effluent CO_2 reached 1% of the feed concentration. Breakthrough times were calculated by subtracting the time to breakthrough using a sample bed packed only with stainless steel beads and cotton plugs from the observed breakthrough time. Then, the breakthrough time of the samples was normalized to 1g for easy comparison from 450 mg of **NJU-Bai52**

crystal, and 490 mg of **NJU-Bai53** crystal.

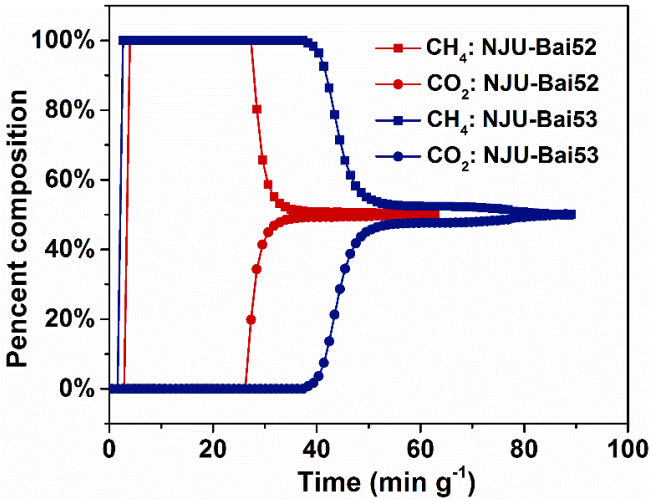

Figure S29. Breakthrough curves for a mixture of CH_4/CO_2 at 298 K.

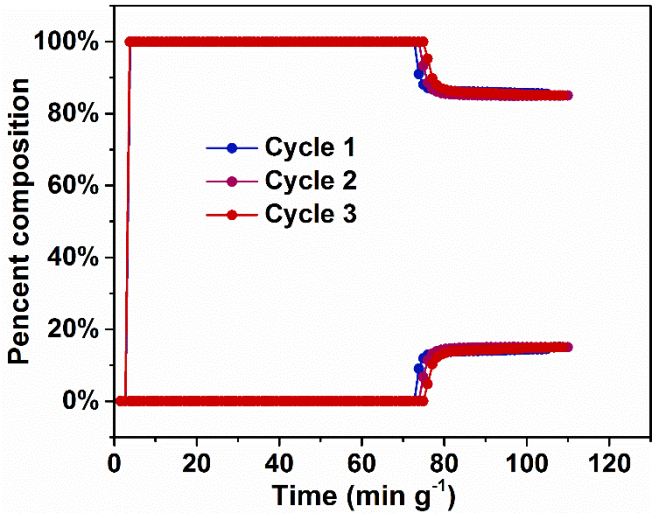

Figure S30. Recyclability of breakthrough tests of N_2/CO_2 on **NJU-Bai52** at 298K.

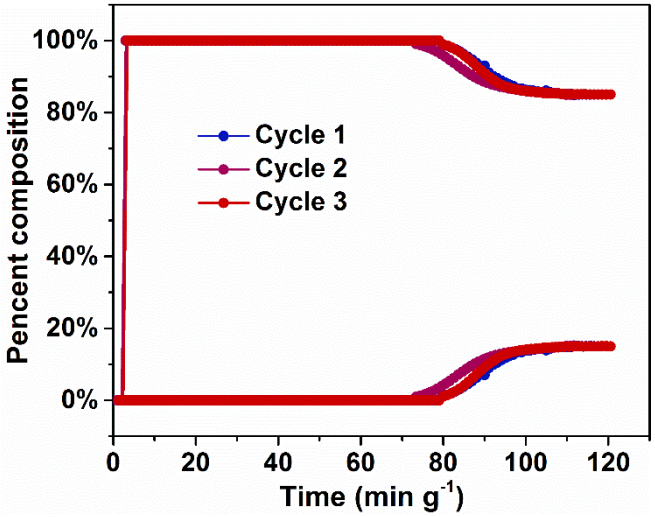

Figure S31. Recyclability of breakthrough tests of N_2/CO_2 on **NJU-Bai53** at 298K.

S16. The computational simulation studies of gases adsorption

To better understand the interaction between the CO_2 molecules and framework and predict the possible binding sites of CO_2 molecules, grand canonical Monte Carlo (GCMC) simulations were carried out through the sorption module of the *Materials Studio 7.0* package according to the literature.[19] The unit-cell framework of **NJU-Bai52** and **NJU-Bai53** were constructed from experimental crystal X-ray diffraction data. The Locate and Metropolis methods[20] were used. The maximum loading and production steps were set as 1×10^5 and 1×10^7, respectively. The simulations were done by utilizing one unit cell, and on the basis of the experimental data (0.15 bar). During the simulation, the CO_2 molecules and framework were considered to be rigid. All atom charges were assigned by the COMPASS force field.[21] The Ewald summation method was used for electrostatic terms. Atom based on van der Waals was included with a 18.5 Å cutoff radius.

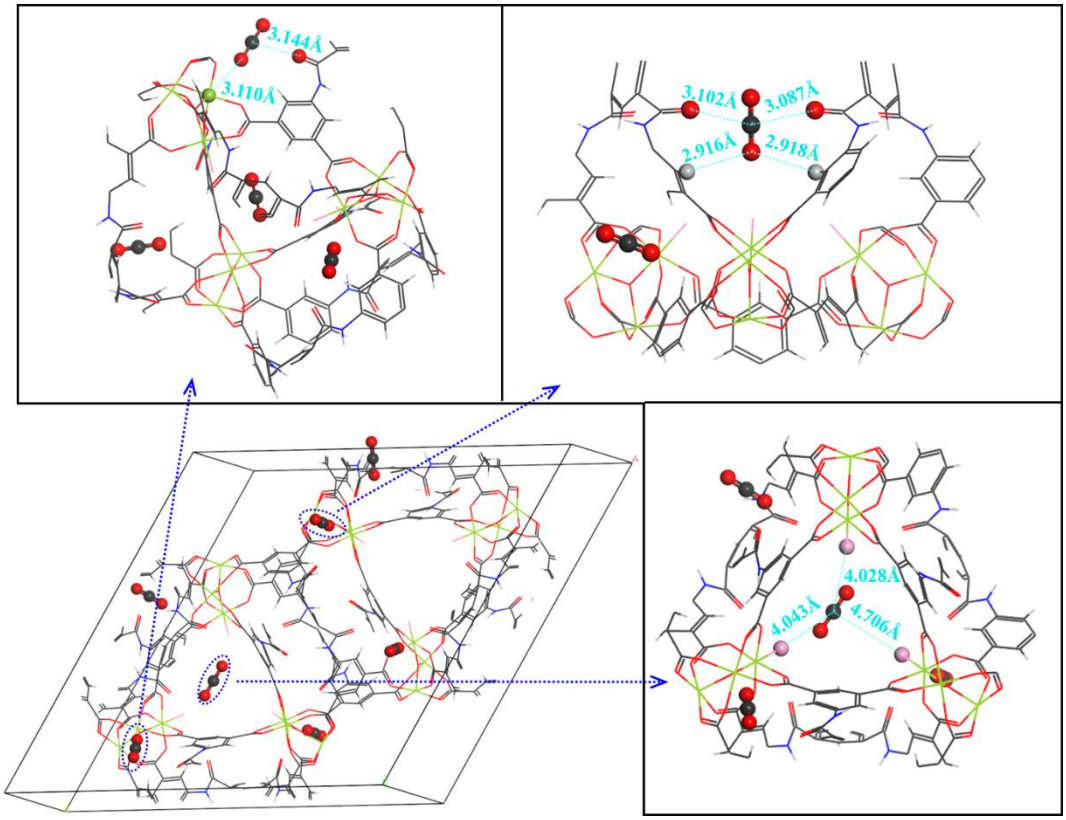

Figure S32. Simulated locations of CO_2 molecules in **NJU-Bai52** at 0.15 bar.

For **NJU-Bai52**, more stable site shows CO_2 at a bridging position between two amide groups (C═O···C = 3.087-3.102 Å) and two aromatic —CH groups (C-H···O = 2.916-2.918 Å). The second CO_2 site is located near one open metal site (Fe···O = 3.110 Å) and one amide group (C═O···C = 3.144 Å). In addition, the CO_2 molecule is also stabilized by weak electrostatic interactions with three chlorine atoms (Cl···C = 4.028-4.706 Å).

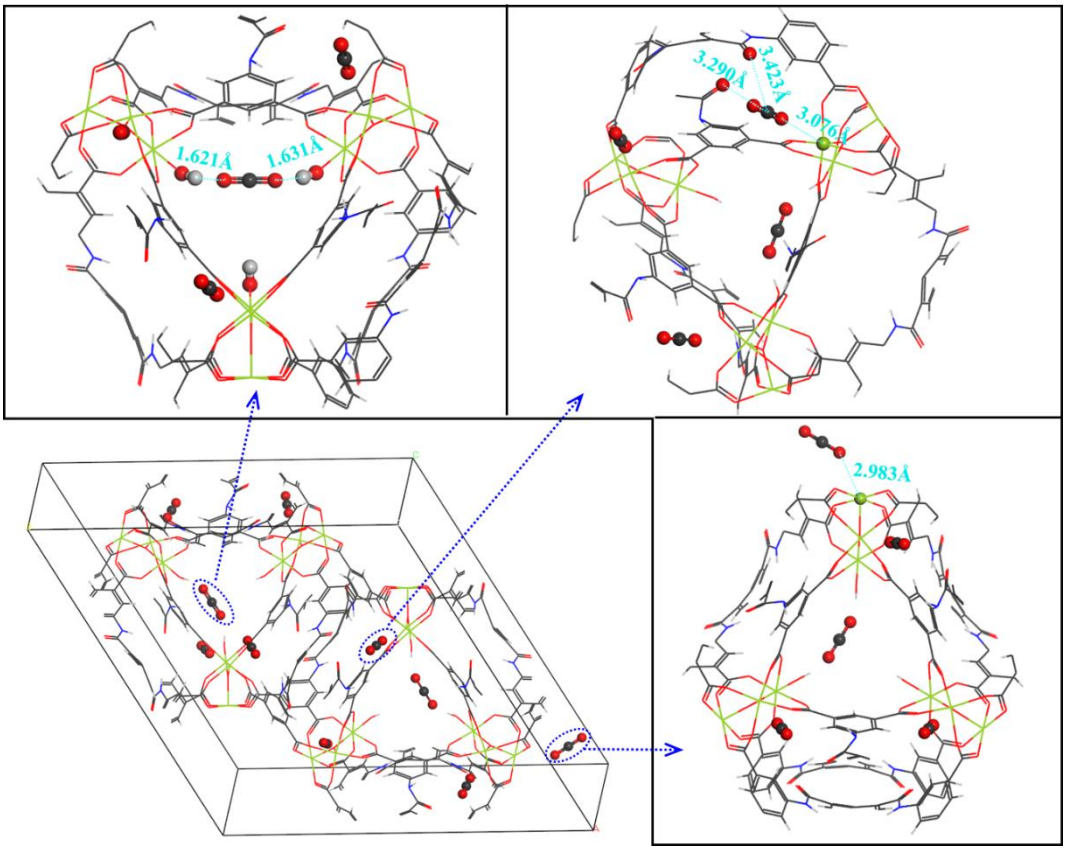

Figure S33. Simulated locations of CO_2 molecules in **NJU-Bai53** at 0.15 bar.

In **NJU-Bai53**, the first, the CO_2 molecule is stuck between two hydroxyl groups (O—H···O = 1.621-1.631 Å), indicative of strong binding interactions between them. the second CO_2 site stabilizes around one open metal site (Fe···O = 3.076 Å) and two amide groups (C═O···C = 3.290-3.423 Å). In addition, some CO_2 molecules also distribute around separate open metal sites (Fe···O = 2.983 Å). Thus, the high CO_2 adsorption of **NJU-Bai53** should be attributed to the simultaneous presence of open metal sites, amide groups, and monodentate hydroxide that provide multiple CO_2 binding sites.

S17. References

(1) Zheng, B.; Bai, J.; Duan, J.; Wojtas, L.; Zaworotko, M. J. Enhanced CO_2 binding affinity of a high-uptake rht-type metal-organic framework decorated with acylamide groups. *J. Am. Chem. Soc.* **2011**, 133, 748-751.

(2) Sheldrick, G. M. A short history of SHELX. *Acta Cryst. Sect. A* **2008**, 64, 112-122.

(3) Spek, A. L. Single-crystal structure validation with the program PLATON. *J. Appl. Cryst.* **2003**, 36, 7-13.

(4) Ibarra, I. A.; Lin, X.; Yang, S.; Blake, A. J.; Walker, G. S.; Barnett, S. A.; Allan, D. R.; Champness, N. R.; Hubberstey, P.; Schroder, M. Structures and H_2 adsorption properties of porous scandium metal-organic frameworks. *Chem. Eur. J.* **2010**, 16, 13671-13679.

(5) (a) Walton, K. S.; Snurr, R. Q. Applicability of the BET Method for Determining Surface Areas of Microporous Metal-Organic Frameworks. *J. Am. Chem. Soc.* **2007**, 129, 8552-8556. (b) Rouquerol, J.; Llewellyn, P.; Rouquerol, F. Is the bet equation applicable to microporous adsorbents? *Stud. Surf. Sci. Catal.* **2007**, 160, 49-56.

(6) Rowsell, J. L. C.; Yaghi, O. M. Effects of Functionalization, Catenation, and Variation of the Metal Oxide and Organic Linking Units on the Low-Pressure Hydrogen Adsorption Properties of Metal-Organic Frameworks. *J. Am. Chem. Soc.* **2006**, 128, 1304-1315.

(7) (a) MYERS, A. L.; PRAUSNITZ, J. M. Thermodynamics of Mixed-Gas Adsorption. *AIChE J.* **1965**, 11, 121-126. (b) Bae, Y.-S.; Mulfort, K. L.; Frost, H.; Ryan, P.; Punnathanam, S.; Broadbelt, L. J.; Hupp, J. T.; Snurr, R. Q. Separation of CO_2 from CH_4 Using Mixed-Ligand Metal-Organic Frameworks. *Langmuir* **2008**, 24, 8592-8598. (c) Mu, B.; Li, F.; Walton, K. S. A novel metal-organic coordination polymer for selective adsorption of CO_2 over CH_4. *Chem. Commun.* **2009**, 2493-2495.

(8) Du, L.; Lu, Z.; Zheng, K.; Wang, J.; Zheng, X.; Pan, Y.; You, X.; Bai, J. Fine-tuning pore size by shifting coordination sites of ligands and surface polarization of metal-organic frameworks to sharply enhance the selectivity for CO_2. *J. Am. Chem. Soc.* **2013**, 135, 562-565.

(9) Nugent, P.; Belmabkhout, Y.; Burd, S. D.; Cairns, A. J.; Luebke, R.; Forrest, K.; Pham, T.; Ma, S.; Space, B.; Wojtas, L.; Eddaoudi, M.; Zaworotko, M. J. Porous materials with optimal adsorption thermodynamics and kinetics for CO_2 separation. *Nature* **2013**, 495, 80-84.

(10) (a) Caskey, S. R.; Wong-Foy, A. G.; Matzger, A. J. Dramatic Tuning of Carbon Dioxide Uptake via Metal Substitution in a Coordination Polymer with Cylindrical Pores. *J. Am. Chem. Soc.* **2008**, 130, 10870-10871. (b) Mason, J. A.; Sumida, K.; Herm, Z. R.; Krishna, R.; Long, J. R. Evaluating metal–organic frameworks for post-combustion carbon dioxide capture via temperature swing adsorption. *Energy Environ. Sci.* **2011**, 4, 3030-3040. (c) Xiang, S.; He, Y.; Zhang, Z.; Wu, H.; Zhou, W.; Krishna, R.; Chen, B. Microporous metal-organic framework with potential for carbon dioxide capture at ambient conditions. *Nat. Commun.* **2012**, 3, 954.

(11) Liao, P.-Q.; Chen, H.; Zhou, D.-D.; Liu, S.-Y.; He, C.-T.; Rui, Z.; Ji, H.; Zhang, J.-P.; Chen, X.-M. Monodentate hydroxide as a super strong yet reversible active site for CO_2 capture from high-humidity flue gas. *Energy Environ. Sci.* **2015**, 8, 1011-1016.

(12) Jiang, J.; Lu, Z.; Zhang, M.; Duan, J.; Zhang, W.; Pan, Y.; Bai, J. Higher Symmetry Multinuclear Clusters of Metal-Organic Frameworks for Highly Selective CO_2 Capture. *J. Am. Chem. Soc.* **2018**, 140, 17825-17829.

(13) McDonald, T. M.; D'Alessandro, D. M.; Krishna, R.; Long, J. R. Enhanced carbon dioxide capture

upon incorporation of N,N'-dimethylethylenediamine in the metal-organic framework CuBTTri. *Chem. Sci.* **2011**, 2, 2022-2028.

(14) Song, X.; Zhang, M.; Duan, J.; Bai, J. Constructing and finely tuning the CO_2 traps of stable and various-pore-containing MOFs towards highly selective CO_2 capture. *Chem. Commun.* **2019**, 55, 3477-3480.

(15) Shekhah, O.; Belmabkhout, Y.; Chen, Z.; Guillerm, V.; Cairns, A.; Adil, K.; Eddaoudi, M. Made-to-order metal-organic frameworks for trace carbon dioxide removal and air capture. *Nat. Commun.* **2014**, 5, 4228.

(16) McDonald, T. M.; Lee, W. R.; Mason, J. A.; Wiers, B. M.; Hong, C. S.; Long, J. R. Capture of carbon dioxide from air and flue gas in the alkylamine-appended metal-organic framework mmen-Mg_2(dobpdc). *J. Am. Chem. Soc.* **2012**, 134, 7056-7065.

(17) Lee, W. R.; Hwang, S. Y.; Ryu, D. W.; Lim, K. S.; Han, S. S.; Moon, D.; Choi, J.; Hong, C. S. Diamine-functionalized metal–organic framework: exceptionally high CO_2 capacities from ambient air and flue gas, ultrafast CO_2 uptake rate, and adsorption mechanism. *Energy Environ. Sci.* **2014**, 7, 744-751.

(18) (a) Jee, J.-G.; Kim, M.-B.; Lee, C.-H. Adsorption Characteristics of Hydrogen Mixtures in a Layered Bed: Binary, Ternary, and Five-Component Mixtures. *Ind. Eng. Chem. Res.* **2001**, 40, 868-878. (b) Britt, D.; Furukawa, H.; Wang, B.; Glover, T. G.; Yaghi, O. M. Highly efficient separation of carbon dioxide by a metal-organic framework replete with open metal sites. *Proc. Natl. Acad. Sci.* **2009**, 106, 20637-20640. (c) Bae, Y.-S.; Lee, C. Y.; Kim, K. C.; Farha, O. K.; Nickias, P.; Hupp, J. T.; Nguyen, S. T.; Snurr, R. Q. High propene/propane selectivity in isostructural metal-organic frameworks with high densities of open metal sites. *Angew. Chem. Int. Ed.* **2012**, 51, 1857-1860. (d) Grant Glover, T.; Peterson, G. W.; Schindler, B. J.; Britt, D.; Yaghi, O. MOF-74 building unit has a direct impact on toxic gas adsorption. *Chem. Eng. Sci.* **2011**, 66, 163-170. (e) Bereciartua, P. J.; Cantín, Á.; Corma, A.; Jordá, J. L.; Palomino, M.; Rey, F.; Valencia, S.; Jr., E. W. C.; Kortunov, P.; Ravikovitch, P. I.; Burton, A.; Yoon, C.; Wang, Y.; Paur, C.; Guzman, J.; Bishop, A. R.; Casty, G. L. Control of zeolite framework flexibility and pore topology for separation of ethane and ethylene. *Science* **2017**, 358, 1068-1071.

(19) Li, Y. W.; Yan, H.; Hu, T. L.; Ma, H. Y.; Li, D. C.; Wang, S. N.; Yao, Q. X.; Dou, J. M.; Xu, J.; Bu, X. H. Two microporous Fe-based MOFs with multiple active sites for selective gas adsorption. *Chem. Commun.* **2017**, 53, 2394-2397.

(20) Metropolis, N.; Ulam, S. The Monte Carlo Method. *J. Am. Stat. Assoc.* **1949**, 44, 335-341.

(21) Sun, H. COMPASS: An ab Initio Force-Field Optimized for Condensed-Phase Applications Overview with Details on Alkane and Benzene Compounds. *J. Phys. Chem. B* **1998**, 102, 7338-7364.